TOTAL VARIATION WAVELET INPAINTING *

TONY F. CHAN †, JIANHONG SHEN ‡, AND HAO-MIN ZHOU §

Abstract. We consider the problem of filling in missing or damaged wavelet coefficients due to lossy image transmission or communication. The task is closely related to classical inpainting problems, but also remarkably differs in that the inpainting regions are in the wavelet domain. New challenges include that the resulting inpainting regions in the pixel domain are usually not well defined, as well as that degradation is often spatially inhomogeneous. Two novel variational models are proposed to meet such challenges, which combine the total variation (TV) minimization technique with wavelet representations. The associated Euler-Lagrange equations lead to nonlinear partial differential equations (PDE's) in the wavelet domain, and proper numerical algorithms and schemes are designed to handle their computation. The proposed models can have effective and automatic control over geometric features of the inpainted images, including the sharpness and curvature information of edges.

1. Introduction. Image inpainting refers to filling in missing or damaged regions (like cracks or scars) in images. In fine art museums, inpainting of degraded paintings is traditionally carried out by professional artists and usually very time consuming, not to mention the risk of completely destroying a precious and world-unique ancient painting due to direct retouching.

Mathematically speaking, inpainting is essentially an interpolation problem, and thus directly overlaps with many other important tasks in computer vision and image processing, including image replacement [35], disocclusion [39], and error concealment [36] [51]. The current work has been more motivated and inspired by the error concealment application, which is to automatically recover lost (image) information during transmission processes.

The notion of *digital image inpainting* was invented by Bertalmio-Sapiro-Caselles-Balleste in [3], where the authors pioneered a novel inpainting technique based on a 3rd order nonlinear PDE. This work has stimulated the recent wave of interest in geometric image interpolation and inpainting problems, for example, variational PDE models [9], [10], [11], [28], Navier-Stokes equation and fluid dynamic system related methods [2], landmark based inpainting [37], texture inpainting [4], inpainting by vector fields and gray levels [1], and inpainting by corresponding maps [22]. Very recently, PDE techniques in image inpainting were featured in the article "Filling in Blanks" by Ivars Peterson in the **Science News** (Vol. 161/19, 05/11/2002) [45].

In this paper, we study wavelet based image inpainting problems, which are different from traditional image inpainting problems. We consider missing or damaged regions in the wavelet domain, instead of the pixel domain in which traditional inpainting problems are defined. The primary motivation for us to study wavelet based image inpainting is that many images are formatted and stored in terms of wavelet coefficients, especially after the release of the new image compression standard JPEG2000, which is largely based on wavelet transforms, including the famous Daubechies 7-9 biorthogonal wavelet decomposition. Minor damages to compact discs

*Research supported in part by grants ONR-N00014-03-1-0888, NSF DMS-9973341 and DMS-0202565, and NIH contract P 20 MH65166.

† Department of Mathematics, the University of California, Los Angeles, CA90095-1555. email:chan@math.ucla.edu.

‡ Department of Mathematics, the University of Minnesota, 206 Church St. SE Minneapolis, MN 55455. email:jhshen@math.umn.edu.

§ School of Mathematics, Georgia Institute of Technology, Atlanta, GA 30332. email:hmzhou@math.gatech.edu.

coding JPEG2000 image files and data loss during wireless transmission processes, for example, could both result in the need for filling-in the missing information in the wavelet domain instead of the pixel domain.

Working on the wavelet domain, instead of the pixel domain, changes the nature of the inpainting problem, since damages to wavelet coefficients can create correlated damage patterns in the pixel domain. For instance, for wavelets based image inpainting problems, there is usually no corresponding clear cut inpainting regions, which is however necessary for most existing PDE based inpainting models in pixel domains. A direct consequence of this lack of geometric regularity of inpainting regions is the prohibition of geometric interpolation techniques in pixel domains [39]. On the other hand, direct interpolation in the wavelet domain is also problematic, as wavelet coefficients (except the low frequencies) are calculated to decouple the correlation between neighboring pixels. Retained high frequency coefficients provide minimal information for the missing coefficients.

For this reason, many contemporary error concealment methods for JPEG (built upon discrete cosine transforms (DCT)) or JPEG2000 (upon wavelets) images require the additional control of regularity in pixel domains, in addition to direct operations in transformed domains (i.e., DCT or wavelets). Such examples include Hemami-Gray's bi-cubic Coons surface [34], non-uniform rational B-spline (NURBS) by Park-Lee [44] and by Cheng et. al. [18], Niu-Poston's harmonic postprocessing techniques [43], Sapiro and collaborators' separate reconstruction techniques for structures and textures [47], and least square minimization in wavelet-domain reconstructions [46]. However, these JPEG based error concealment methods usually work on images that have already been partitioned into 8×8 or 16×16 blocks. Each missing or damaged block corresponds to a well defined square region to be filled-in in the pixel domain. This is different from our current work, for which no assumption is made of the block partitioning.

Depending on the scales or resolutions, missing or damaged wavelet coefficients could cause degradation wide spread in the pixel domain. That is, even a few coefficients can potentially affect all pixels. Moreover, unlike denoising problems in which the perturbation in the pixel domain is mostly homogeneous, the degradation in wavelet inpainting problems is usually inhomogeneous (different regions can suffer different level of damages). This new phenomenon demands different treatments in different regions in the pixel domain.

These novel features and challenges call for new models and methods of image inpainting in the wavelet domain. An important guiding principle for us is that even though the primary goal is to fill in the missing coefficients in the wavelet domain, it is important to control the regularity in the pixel domain, so that the inpainted images retain important geometrical features, especially when noise is present.

Such considerations have motivated the variational PDE approach in our current work. The variational PDE technique has been widely used in numerous applications such as image segmentation [7] [13] [52], restoration [14], [48], and compression [16] [26]. Even for traditional image inpainting, PDE methods have been well studied [3] [9] [11] [28] [2].

The growing impact of PDE techniques in image processing is mainly due to their capability in controlling geometrical features of images. PDE's (many of them are derived from variational principles) are usually designed to possess certain desirable geometrical properties. For example, total variation (TV) minimization, which leads to a curvature term in the corresponding Euler-Lagrange equation, can retain sharp

edges in image restoration. In this paper, we select TV minimization to facilitate the inpainting process so that the missing or damaged coefficients can be filled in to faithfully restore geometric image features. In addition, the TV minimization can also systematically suppress the noise in the images. All the above properties make TV minimization a crucial ingredient for wavelets based image inpainting.

In this paper, unlike most conventional TV minimization techniques in image processing, the total variation regularity is directly imposed on the wavelet domain. The idea of using TV minimization together with wavelet representations in image processing has been proposed by different research groups. For example, in an earlier work of the first two authors [17], models of combining wavelets and TV minimization have been studied for image denoising and compression. Later, Durand-Froment [27] use TV minimization in conjunction with wavelets to eliminate pseudo oscillations in image restoration, and Candes-Guo [6] use TV minimization to clean up oscillations from curvelet reconstructions.

This paper is arranged as follows. In Section 2, we give two models for the wavelet based inpainting problems according to the presence or absence of noise. In Section 3, we derive the Euler-Lagrange equations for the models and analyze their relationships to other wavelets based image processing tasks. We also prove existence of the solutions and give an example to illustrate the non-uniqueness of the solutions. Section 4 presents numerical algorithms and schemes for solving the Euler-Lagrange equations. Generic numerical examples in Section 5 further highlight the remarkable inpainting qualities of both the models and their numerical schemes.

2. TV Minimization Models for Wavelets Based Image Inpainting. In this section, we propose two TV regularized wavelet based image inpainting models depending on whether or not noise needs to be suppressed in the image.

We start with a standard image model,

$$z(x) = u_0(x) + n(x), \tag{1}$$

where $u_0(x)$ is the original noise free image and $n(x)$ the Gaussian white noise with $\|n(x)\|_2 = \sigma$, and σ is a constant related to the noise level. We assume that the size of the image is $n \times m$. Let us denote the standard wavelet transform of $z(x)$ by,

$$z(\alpha, x) = \sum_{j,k} \alpha_{j,k} \psi_{j,k}(x), \qquad j \in \mathbf{Z},\ k \in \mathbf{Z}^2. \tag{2}$$

(For tensor-product based multiresolution analysis in 2-D, there should be three mother wavelets $\psi^{(1)}, \psi^{(2)}$, and $\psi^{(3)}$, but for convenience we shall instead only use a single symbol ψ. No confusion will arise below since both our models and algorithms will not differentiate between them.) In wavelet based image representations, the coefficients $\alpha = \{\alpha_{j,k}\}$ are the values being stored. Notice that here the low and high frequency (or scale) coefficients are not being distinguished, while standard digital representations usually need to separate them. One reason to do so is for simplicity. A different reason is that in the proposed models and methods, we allow the missing or damaged coefficients to be in both the low and high frequency ranges. The models can automatically handle them differently if they belong to different frequency ranges, even though low frequency coefficients have completely different properties than the high frequency ones.

Damages (scratches and scars) in the wavelet domain cause loss of wavelet coefficients of $z(x)$ on the index region I, i.e., $\{\alpha_{j,k}\}$'s with $(j,k) \in I$ represent those

wavelet components missing or damaged. The task of inpainting is to restore the missing coefficients in a *proper* manner, so that the image will have as much information being restored as possible.

As mentioned before, the inpainting problem usually allows more than one solutions and many different ways to fill in the missing coefficients, which lead to different reconstructions in the pixel domain. One often has to use proper regularization to guide the filling of missing coefficients. In many applications, it is crucial to have geometrical features (from available image information) propagated into the pixel domains of inpainting. For this reason, it is important to control the regularity in the pixel domain, so that broken or incomplete edges can be completed faithfully, and noise removed effectively.

With all these factors in mind, we now propose two variational models for wavelets based image inpainting.

If the target image is noiseless or the noise n is small enough to be negligible, one just needs to fill in the damaged wavelet coefficients and preserve the other coefficients. We propose a simple TV minimization scheme to fill in the missing coefficients.

Model I (for noiseless images):

$$\min_{\beta_{j,k}:(j,k)\in I} F(u,z) = \int_{\mathbf{R}^2} |\nabla_x u(\beta,x)|dx = \mathrm{TV}(u(\beta,x)), \tag{3}$$

where $u(\beta,x)$ has the wavelet transform:

$$u(\beta,x) = \sum_{j,k} \beta_{j,k}\psi_{j,k}(x), \qquad \beta = (\beta_{j,k}), \quad j \in \mathbf{Z},\ k \in \mathbf{Z}^2,$$

and subject to the constraint:

$$\beta_{j,k} = \alpha_{j,k}, \quad (j,k) \notin I,$$

where I is the inpainting index region. We remark that the derivative ∇u is often denoted by the Radon measure symbol Du in the standard literature on functions with bounded variations (BV).

In many applications, such as signal transmission in wireless channels, noise is unavoidably introduced in addition to the loss of data packages. More precisely, in addition to the possibility that some coefficients $\beta_{j,k}, (j,k) \in I$ can be completely lost or damaged, the remaining others $(\beta_{j,k}, (j,k) \notin I)$ can also be polluted by noise, which cannot be ignored. In this situation, we propose a second model for wavelet inpainting.

Model II (for noisy images):

$$\min_{\beta_{j,k}} F(u,z) = \int_{\mathbf{R}^2} |\nabla_x u(\beta,x)|dx + \sum_{(j,k)} \lambda_{j,k}(\beta_{j,k} - \alpha_{j,k})^2, \tag{4}$$

and the parameter $\lambda_{(j,k)}$ is zero if $(j,k) \in I$, the missing index set; otherwise, it equals a positive constant λ to be properly selected (see further discussions in the next section).

In the objective functions in (3) and (4), we use the total variation (TV) norm because it can retain sharp edges while reducing the noise and other oscillations, such as Gibbs' phenomena, in the reconstruction [48]. Our approach can be easily extended to include other regularizers, such as ones containing curvature [9]

The models are related to our earlier studies of TV model for wavelet based image denoising and compression [17]. The key difference between the models is that in Model I, the arguments in the TV minimization are restricted to the inpainting regions I only, the dimension of unknowns is the number of coefficients in I, while in Model II, the parameter λ is taken to be zero in the inpainting regions in the wavelet domain, in contrast to the standard denoising and compression models, where λ is usually taken to be a constant. This difference essentially puts no constraint on the missing wavelet coefficients so that they can change freely, and therefore restore the missing information.

We remark that unlike most image processing models, Model I does not require any user-defined parameter. This provides significant advantages for Model I over the other TV based image processing models. Of course, the preassumption for Model I is that the given image observation, or equivalently the available collection of its wavelet coefficients, is noiseless.

3. Analysis of the Models. For convenience, we shall assume in this section that the image domain is the entire plane $\Omega = \mathbf{R}^2$, and the gradient symbol ∇u represents $\nabla_x u(\beta, x)$. As common in the variational literature, the image u is always assumed to be smooth so that all the subsequent formal derivations of the Euler-Lagrange equations can be valid in the classical sense.

3.1. Euler-Lagrange Equations. Let

$$\beta_I = \{\beta_{j,k} \mid (j,k) \in I\}$$

denote all the missing wavelet coefficients to be inpainted. Since it has been assumed that $\#I = d$, β_I can be considered as a vector in $\mathbf{R}^d$.

For Model I, one attempts to minimize

$$F(\beta_I) = F(u, z) = \int_{\mathbf{R}^2} |\nabla u(\beta, x)| dx.$$

For any missing index $(j,k) \in I$,

$$\begin{aligned} \frac{\partial F(\beta_I)}{\partial \beta_{j,k}} &= \int_{\mathbf{R}^2} \frac{\nabla u}{|\nabla u|} \cdot \frac{\partial \nabla u(\beta, x)}{\partial \beta_{j,k}} dx \\ &= \int_{\mathbf{R}^2} \frac{\nabla u}{|\nabla u|} \nabla \frac{\partial u(\beta, x)}{\partial \beta_{j,k}} dx \\ &= \int_{\mathbf{R}^2} \frac{\nabla u}{|\nabla u|} \cdot \nabla \psi_{j,k} dx. \end{aligned} \tag{5}$$

Equivalently, if one assumes that the mother wavelet ψ is compactly supported (as for Daubechies family of wavelets [20]) and at least Lipschitz continuous, integration-by-parts yields

$$\frac{\partial F(\beta_I)}{\partial \beta_{j,k}} = -\int_{\mathbf{R}^2} \nabla \cdot \left[\frac{\nabla u}{|\nabla u|} \right] \psi_{j,k} dx = -\langle \kappa, \psi_{j,k} \rangle, \tag{6}$$

where $\kappa = \nabla \cdot [\nabla u / |\nabla u|]$ is the celebrated curvature formula for the level lines of u. Thus this last formula clearly combines geometric information with wavelets decomposition.

Formula (5) on the other hand bears the advantage that it is well defined in the classical sense as long as both the mother wavelet ψ and the image u are Lipschitz continuous. That is, unlike formula (6), the image u needs not to be $C^{1,1}$. Furthermore, the differential $\nabla\psi_{j,k}$ also possesses the similarity relation:

$$\nabla\psi_{j,k}(x) = 2^j(\nabla\psi)_{j,k}, \quad x \in \mathbf{R}^2,\ k \in \mathbf{Z}^2.$$

Accordingly, it suffices to compute $\nabla\psi$ only once for the mother wavelet, and the rest can be obtained algebraically by dilation and translation.

It is also now a standard regularization technique to replace $|\nabla u|$ in the denominators of (5) and (6) by:

$$|\nabla u|_\epsilon = \sqrt{|\nabla u|^2 + \epsilon}, \qquad \text{with} \quad 0 < \epsilon \ll 1.$$

The small positive regularizer ϵ prevents the denominators from vanishing in numerical implementations. In fact, define the minimum-surface type of energy:

$$F_\epsilon(\beta_I) = \int_{\mathbf{R}^2} |\nabla u(\beta, x)|_\epsilon dx.$$

Then

$$\frac{\partial F_\epsilon(\beta_I)}{\partial \beta_{j,k}} = \int_{\mathbf{R}^2} \frac{\nabla u}{|\nabla u|_\epsilon} \cdot \nabla\psi_{j,k} dx = -\int_{\mathbf{R}^2} \nabla \cdot \left[\frac{\nabla u}{|\nabla u|_\epsilon}\right] \psi_{j,k} dx,$$

which are precisely the ϵ-regularized versions of (5) and (6). Our later computational schemes will be based on such regularization.

Similarly, for Model II with homogeneous Gaussian white noise, one can repeat the above computation and obtain, for any (j,k),

$$\begin{aligned}\frac{\partial F(\beta_I)}{\partial \beta_{j,k}} &= \int_{\mathbf{R}^2} \frac{\nabla u}{|\nabla u|} \cdot \nabla\psi_{j,k} dx + 2\lambda_{j,k}(\beta_{j,k} - \alpha_{j,k}) \\ &= -\int_{\mathbf{R}^2} \nabla \cdot \left[\frac{\nabla u}{|\nabla u|}\right] \psi_{j,k} dx + 2\lambda_{j,k}(\beta_{j,k} - \alpha_{j,k}).\end{aligned}$$

Here $\lambda_{j,k}$ is the binary function over indices:

$$\lambda_{j,k} = 0, \quad (j,k) \in I; \quad \lambda, \qquad \text{otherwise.} \tag{7}$$

Treating λ as a function on indices introduces more adaptivity or flexibility into most inpainting models [10] [9] [28]. For instance, if the noise is not spatially homogeneous so that the noise variance σ^2 on the wavelet coefficients are component-dependent:

$$\sigma^2 = \sigma^2_{j,k}, \quad \forall (j,k),$$

then instead of the binary choice in (7), one could allow λ to be a general function of indices with:

$$\lambda_{j,k} = 0, \quad (j,k) \in I; \quad \propto \frac{1}{\sigma^2_{j,k}}, \qquad \text{otherwise.}$$

In particular, if $\sigma_{j,k} = 0$ and the coefficients are noiseless, it reproduces Model I: for $(j,k) \in I$, $\lambda_{j,k} = 0$, and

$$-\int_{\mathbf{R}^2} \nabla \cdot \left[\frac{\nabla u}{|\nabla u|}\right] \psi_{j,k} dx = 0; \tag{8}$$

otherwise (corresponding to all the available noiseless coefficients), $\lambda_{j,k} = \infty$ and $\beta_{j,k} = \alpha_{j,k}$. Equation (8) is usually called the Euler-Lagrange equation for Model I.

Similarly, one can obtain the Euler-Lagrange equation for Model II as

$$-\int_{\mathbf{R}^2} \nabla\left(\frac{\nabla u}{|\nabla u|}\right)\psi_{j,k}(x)dx + 2\lambda_{j,k}(\beta_{j,k} - \alpha_{j,k}) = 0. \tag{9}$$

In Section 4, we shall detail on the numerical computation of these two models.

3.2. Why the Hybrid Models. From the wavelet representation point of view, one naturally asks the following question:

"Can both models be expressed explicitly by the wavelet representation?"

More specifically, as in the celebrated denoising works by Donoho, DeVore, and their collaborators [24, 25, 21, 8], is there an *equivalent* model (to Model II, say) that is fully based on the wavelet coefficients in the classical form of:

$$F^*(\beta) = \Phi(|\beta_{j,k}|'s) + \sum_{(j,k)} \lambda_{j,k}(\beta_{j,k} - \alpha_{j,k})^2,$$

where $(|\beta_{j,k}|'s)$ denotes the sizes of all wavelet coefficients, and Φ a suitable function of all these sizes. By *equivalence* to model II, we mean there exist two fixed positive constants C_1 and C_2, independent of β or u, so that

$$C_1\mathrm{TV}(u(\beta, x)) \le \Phi(|\beta_{j,k}|'s) \le C_2\mathrm{TV}(u(\beta, x)). \tag{10}$$

The answer is negative, which reveals the major difference between our models and the classical wavelets denoising schemes based on Besov regularity conditions [8, 41]. Recall that the Besov regularity norm is defined by

$$\begin{aligned}\|u\|_{\dot{B}^{\alpha}_{q}(L^p(\mathbf{R}^2))} &= \left(\int_0^\infty (\omega_p(u,h)h^{-\alpha})^q \, dh/h\right)^{1/q} \\ &\sim \left(\sum_j 2^{jq(\alpha+1-2/p)}\|\beta_j,\|^q_{l^p}\right)^{1/q}.\end{aligned}$$

Here the dot symbol in $\dot{B}^{\alpha}_{q}(L^p(\mathbf{R}^2))$ indicates the homogeneity of the Besov norm in discussion, $\|\beta_j,\|_{l^p}$ the sequence l^p-norm at each resolution j, and ω the p-modulus of continuity:

$$\omega_p(f,h) = \sup_{|a|\le h} \|f(x+a) - f(x)\|_{L^p(\mathbf{R}^2)}.$$

In fact, one has the following negative result for images with bounded variations [41].

THEOREM 3.1. *The space of $BV(\mathbf{R}^2)$ cannot be characterized by size properties on wavelet coefficients.*

The wavelet coefficients vector β of a BV image lies somewhere between l^1 and weak l^1, according to the results of Yves Meyer [41], and Albert Cohen et al. [19].

The fact that a generic image of BV is beyond simple wavelet description is mainly due to the geometric nature of the total variation norm, or more generally, the total variation as a Radon measure [31]. The preceding discussion has already revealed that the first variation of the total variation measure leads to the most important second order Euclidean geometric feature - the curvature

$$\kappa = \kappa(\beta, x) = \nabla \cdot \left[\frac{\nabla u(\beta, x)}{|\nabla u(\beta, x)|} \right].$$

Even more profound on the geometric nature of the total variation regularizer is the celebrated co-area formula of Fleming-Rishel [29] and De Giorgi [30]:

$$\int_{\mathbf{R}^2} |\nabla u| dx = \int_{-\infty}^{\infty} \text{length}(\text{u} \equiv \gamma) \text{d}\gamma, \tag{11}$$

where $u \equiv \gamma$ denotes the γ-level curve for any $\gamma \in \mathbf{R}^2$. Therefore, the total variation Radon measure $|\nabla u|$ amounts to summing up the lengths of *all* the level lines of a given image u. For simplicity, u has been assumed to be smooth so that its level lines are well defined. For more general images with bounded variation, the above coarea formula can be updated to

$$\int_{\mathbf{R}^2} |Du| = \int_{-\infty}^{\infty} \text{Per}(\text{u} > \gamma) \text{d}\gamma.$$

Here $|Du|$ denotes total variation as a Radon measure, and $\text{Per}(\text{u} > \gamma)$ the perimeter of the Caccioppli set [31]

$$\{x \in \mathbf{R}^2 \mid u(x) > \gamma\}.$$

Classical wavelets, as space-scale representation tools, are however not originally motivated by, nor designed to handle explicitly, geometric information. This could at least shed some light on why generic BV images are beyond explicit descriptions based upon only the sizes of their wavelet coefficients. Many researchers have noticed this drawback, and proposed different ways to incorporate geometries in the study. Nowadays, geometric harmonic analysis, e.g. curvelets [5], is a hot research topic.

On the other hand, in computer vision as well as human vision, geometric information in images, such as edges, smoothness, junctions, and corners, are significant visual cues for successful perception (see, e.g., David Marr's work [40]). The space of functions with bounded variations, among all the familiar functional spaces in classical real analysis, is perhaps the simplest one that *legalizes* the existence of jumps or edges. Other image models such as the celebrated Mumford-Shah's object-edge model [42], often substantially increase the complexity in both theory and computation, by explicitly singling out the edge geometric feature.

To conclude, with wavelet coefficients inevitably polluted by noise and partially missing, it seems natural to explicitly enforce the edge geometric information using the total variation Radon measure. Such hybrid models (e.g., Model I and Model II) can faithfully inpaint the missing wavelet coefficients while retaining the sharpness of missing edges. Our later numerical results shall further confirm our claim.

3.3. Existence Theorems of Model I and II. In this section, we prove the existence theorems for both models I and II. The non-uniqueness issue will be addressed in the next subsection.

We take an elementary approach for proving the existence of solutions to Model I, while a more general one based on the direct method for Model II. The image domain is assumed to be the entire plane $\mathbf{R}^2$.

Following the preceding notations, let I denote the set of indices associated with all the missing wavelets coefficients and $d = \#I < \infty$, the number of lost coefficients. Define two orthogonally complementing subspaces of $L^2(\mathbf{R}^2)$ according to I:

$$\begin{aligned} V_I &= \text{span}\{\psi_{j,k} \mid (j,k) \in I\}, \\ U_I &= \text{closure}(\text{span}\{\psi_{j,k} \mid (j,k) \notin I\}). \end{aligned}$$

Let Q_I and P_I denote the orthogonal projections onto V_I and U_I separately. Then

$$Q_I + P_I = Id, \qquad \text{the identity operator in } L^2(\mathbf{R}^2),$$

and $z_I = P_I z$ is the available observation while $Q_I z$ is lost during transmission.

We now first turn to the existence of Model I. Any inpainting candidate u can be decomposed to

$$u = u_I + v_I, \quad \text{with } u_I = P_I u, \quad v_I = Q_I u.$$

For Model I, z is assumed to be noiseless and $u_I = P_I z$ is therefore fixed. The only freedom comes from the v_I or β_I component. Write:

$$v_I = v_I(\beta_I, x), \quad \beta_I = \{\beta_{j,k} \mid (j,k) \in I\},$$

to indicate the dependence of v_I on the missing wavelet coefficients β_I. Define

$$F(\beta_I) = F(u, z) = \text{TV}(u_I + v_I(\beta_I, x)).$$

Then $F(\beta_I)$ could be considered as a function on $\mathbf{R}^d$.

THEOREM 3.2. *Assume that the mother wavelet $\psi(x)$ belongs to* $\text{BV}(\mathbf{R}^2)$ *and is compactly supported, which are true for most familiar wavelets (e.g., Haar wavelets, or any C^1 family) [20]. Also assume that u_I belongs to* $\text{BV}(\mathbf{R}^2)$. *Then the objective function $F(\beta_I)$ satisfies*

(a) $F(\beta_I)$ is (Lipschitz-) continuous; and

(b) $F(\beta_I) \to +\infty$ as $\beta_I \to \infty$ in $\mathbf{R}^d$.

As a result, the minimizer to $F(\beta_I)$ must exist.

Proof. By the assumption on the mother wavelet, $\psi_{j,k}$ belongs to $\text{BV}(\mathbf{R}^2)$ for any $(j,k) \in I$. Since TV is a semi-norm, one has for any β_I and β_I' in $\mathbf{R}^d$,

$$\begin{aligned} |F(\beta_I) - F(\beta_I')| &= |\text{TV}(u_I + v_I(\beta_I, x)) - \text{TV}(u_I + v_I(\beta_I', x))| \\ &\le \text{TV}(v_I(\beta_I, x) - v_I(\beta_I', x)) \\ &= \text{TV}(v_I(\beta_I - \beta_I', x)) \\ &\le \|\beta_I - \beta_I'\|_{l^1} \max_{(j,k)\in I} \text{TV}(\psi_{j,k}). \end{aligned}$$

This proves (a) since all norms in $\mathbf{R}^d$ are equivalent. By further noticing that $v_I = Q_I u$ is compactly supported, by Poincaré's inequality [31, 38], one has

$$\int_{\mathbf{R}^2} |v_I|^2 dx \le C \int_{\mathbf{R}^2} |\nabla v_I| dx = C \times \text{TV}(v_I),$$

where the positive constant C is universal and independent of v_I, or equivalently β_I. Thus under a general orthonormal wavelet basis,

$$\begin{aligned} F(\beta_I) &= \mathrm{TV}(u_I + v_I(\beta_I, x)) \\ &\geq \mathrm{TV}(v_I(\beta_I, x)) - \mathrm{TV}(u_I) \\ &\geq c^{-1}\|v_I\|_{L^2}^2 - \mathrm{TV}(u_I) \\ &= c^{-1}\|\beta_I\|_{l^2}^2 - \mathrm{TV}(u_I) \to +\infty, \quad \text{as } \beta_I \to \infty. \end{aligned}$$

This establishes (b) and completes the existence proof for Model I. □

The proof for the existence of Model II inpainting has to take a turn, due to the aforementioned fact that there exists no simple and explicit description for the TV norm in the wavelets domain. A natural way to proceed is to deal with the physical image u directly, instead of its wavelet coefficients β.

Model II is to minimize the energy

$$F(u, z) = \int_{\mathbf{R}^2} |\nabla u| dx + \lambda \int_{\mathbf{R}^2} (u_I - z_I)^2 dx, \tag{12}$$

where $u_I = P_I u$ and $z_I = P_I z$. Unlike most other variational models in image processing, the incompleteness of data imposes a subtle challenge for proving the existence, because the lack of data (in the fitting term) results in an incomplete control over the global norms, which is however often crucial for establishing weak compactness of minimizing sequences in the direct method. For this purpose, Poincaré's inequality on the *entire* plane plays a fundamental role in the following proof.

THEOREM 3.3. *Suppose that the available set of wavelet coefficients α_{I^c} is in l^2, or equivalently,*

$$z_I = P_I z \in L^2(\mathbf{R}^2).$$

Then the minimizer to $F(u, z)$ in Model II (12) exists.

Proof. First, from the assumption it follows that for any admissible inpainting u, its u_I component must belong to $L^2(\mathbf{R}^2)$ due to the fitting term in $F(u, z)$. Since

$$u = Q_I u + P_I u = Q_I u + u_I,$$

and $Q_I u \in V_I \subset L^2(\mathbf{R}^2)$, it follows that an $F(u, z)$-admissible inpainting u must belong to $L^2(\mathbf{R}^2)$.

Since $u = 0$ is apparently admissible, there must exist a minimizing sequence $(u^i)_{i=1}^{\infty}$ for $F(u, z)$. Then $u^i \in L^2(\mathbf{R}^2)$, and

$$\int_{\mathbf{R}^2} |\nabla u^i| dx \leq F(u^i, z) \to \inf_u F(u, z), \quad i \to \infty.$$

In particular, the total variations of u^i's are bounded. Recall Poincaré's inequality in $\mathbf{R}^2$ [31, 38],

$$\int_{\mathbf{R}^2} |u|^2 dx \leq C \int_{\mathbf{R}^2} |\nabla u| dx,$$

for any $u \in L^2(\mathbf{R}^2)$ (whose total variation could be infinity), and a universal constant C independent of u. We thus conclude that (u^i) must be bounded in $L^2(\mathbf{R}^2)$.

As a result, on any *bounded* open domain $\Omega \subset \mathbf{R}^2$, the restriction of (u^i) must be bounded in $\mathrm{BV}(\Omega)$ (according to Schwarz's inequality). By the L^1 pre-compactness of bounded BV functions on finite domains and the diagonal selection procedure, one can find a subsequence of (u^i), still denoted by the same notation for convenience, such that

$$u^i \to u^*, \quad \text{as } i \to \infty \text{ in } L^1_{\mathrm{loc}}(\mathbf{R}^2),$$

for some locally integrable image u^*. In particular,

$$u^i \to u^*, \quad \text{weakly or in the distributional sense on } \mathbf{R}^2.$$

Then by the lower semi-continuity of the total variation semi-norm under L^1_{loc} topology [31], one has

$$\int_{\mathbf{R}^2} |\nabla u^*| dx \le \liminf_{i\to\infty} \int_{\mathbf{R}^2} |\nabla u^i| dx.$$

By the lower semi-continuity of the L^2-norm under the weak topology, one has

$$\int_{\mathbf{R}^2} |u^*|^2 dx \le \liminf_{i\to\infty} \int_{\mathbf{R}^2} |u^i|^2 dx.$$

Finally, since the mother wavelet is assumed to be compactly supported, it is easy to verify that the projection operator P_I maps compactly supported images to still compactly supported ones. As a result, the weak convergence of (u^i) implies

$$u^i_I = P_I u^i \to u^*_I = P_I u^*, \quad \text{weakly on } \mathbf{R}^2.$$

Then the lower semi-continuity of the L^2-norm yields

$$\int_{\mathbf{R}^2} |u^*_I - z_I|^2 dx \le \liminf_{i\to\infty} \int_{\mathbf{R}^2} |u^i_I - z_I|^2 dx.$$

In combination, one concludes that $u^* \in L^2(\mathbf{R}^2)$ is admissible and

$$F(u^*, z) \le \liminf_{i\to\infty} F(u^i, z) = \inf_u F(u, z).$$

Therefore u^* must be a minimizer, and

$$\beta^*_{j,k} = \langle u^*, \psi_{j,k} \rangle, \quad (j,k) \in I,$$

constitute an optimal set of inpainted wavelet coefficients under Model II, which completes the proof. □

3.4. Non-Uniqueness: An Example via Haar Wavelets. In this section, we show by a concrete 1-D example that like most earlier inpainting models (e.g. [10]), the uniqueness of inpainting is generally not guaranteed.

Define a noiseless 1-D signal or image u with an ideal step edge at $x = 1/2$:

$$u(x) = 1_{x \ge 1/2}(x) = H(x - 1/2),$$

where H denotes the canonical 0-1 Heaviside function. Let $\psi = h(x)$ be the mother Haar wavelet:

$$h(x) = 1_{[0,1/2)}(x) - 1_{[1/2,1)}(x),$$

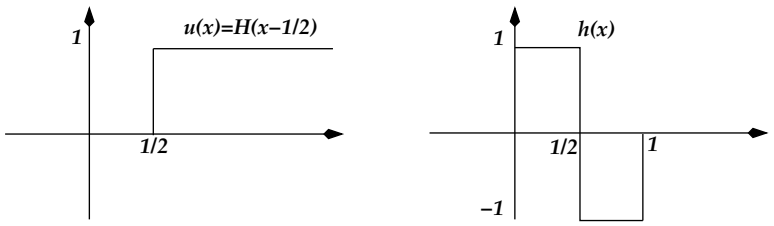

FIG. 1. *A 1-D ideal step-edge image u, and Haar's mother wavelet h(x).*

normalized so that the L^2 norm is 1. Then all other basis wavelets are generated by

$$h_{j,k}(x) = 2^{j/2}h(2^j x - k), \quad j,k \in \mathbf{Z}.$$

Let $\beta_{j,k}$'s denote the wavelet coefficients of the ideal step edge u:

$$\beta_{j,k} = \langle u(x),\ h_{j,k}(x)\rangle = \int_{\mathbf{R}} u(x)h_{j,k}(x)dx.$$

Suppose that a receiver is able to receive all the wavelet coefficients of u, except for the single one

$$\beta_{0,0} = \langle u(x),\ h(x)\rangle = \int_{1/2}^{1}(-1)dx = -\frac{1}{2},$$

which is missing and unknown to the receiver. In this case, the inpainting index set is a singleton $I = \{(0,0)\}$. Define

$$u_I = \sum_{(j,k)\notin I} \beta_{j,k}h_{j,k}(x),$$

which is the reconstruction of u assuming there is no $h_{0,0} = h(x)$ component. Then,

$$u_I(x) = u(x) - \beta_{0,0}h_{0,0}(x) = H(x-\frac{1}{2}) + \frac{1}{2}h(x) = \frac{1}{2}\ 1_{[0,1)}(x) + 1_{[1,\infty)}(x).$$

For each candidate $\beta_{0,0} = a \in \mathbf{R}$, define the reconstruction

$$u(a,x) = u_I(x) + ah(x) \tag{13}$$

$$= (\frac{1}{2}+a)1_{[0,1/2)}(x) + (\frac{1}{2}-a)1_{[1/2,1)}(x) + 1_{[1,\infty)}(x), \tag{14}$$

as in our Model I (since this is a noiseless example). Then Model I is to minimize the following single variable energy:

$$\min_a \int_{\mathbf{R}} |\nabla u(a,x)|dx = \min_a \mathrm{TV}(u(a,x)).$$

Here $|\nabla u|$ is understood in the Radon measure sense since $u(a,x)$ is discontinuous.

Recall in classical real analysis, that the total variation of a piecewise constant function $f(x)$ is precisely the sum of all absolute jumps:

$$\mathrm{TV}(f) = \sum_{x_i\in J} |f(x_i+) - f(x_i-)|,$$

where J denotes the collection of all jumps of f. Since $u(a,x)$ is indeed piecewise constant, we have according to (13), for any $a \in \mathbf{R}$,

$$\mathrm{TV}(u(a,x)) = |1/2+a| + |2a| + |1/2+a| = |1+2a| + |2a|.$$

As a result, the lower bound of the total variation energy is

$$\mathrm{TV}(u(a,x)) \geq |(1+2a) - 2a| = 1,$$

which can be achieved if and only if

$$-1 \leq 2a \leq 0, \qquad \text{or,} \qquad -\frac{1}{2} \leq a \leq 0.$$

In other words, taking any value of $a \in [-\frac{1}{2}, 0]$ minimizes the objective function in Model I, and therefore is a solution of the wavelet inpainting problem. This clearly shows that in this noiseless example, Model I could lead to multiple inpainting results.

We must emphasize, however, as well explained by Chan and Shen in [10], that non-uniqueness is not a drawback of any inpainting model, rather, it is an intrinsic nature of the inpainting problem itself. This distinguishes image inpainting from other familiar image restoration tasks such as image denoising and deblurring.

4. Algorithm. There are many methods available in the literature to find the minimizers of the proposed models. The computation in the current work has been mainly based on the gradient descent approach, which by no means is the most efficient. The primary goal of the present work is however to explore the inpainting feasibility and qualities of the models rather than their numerics.

More precisely, as shown in the previous section, the minimizers of the proposed models satisfy the nonlinear Euler-Lagrange equations (8) and (9). We emphasize that in (8), there are only d equations, where d is the number of coefficients in the inpainting regions I, which can be much smaller than the total number of pixels, leading to more efficient solution procedures.

To find the minimizers, one just needs to solve for the solutions of the above Euler-Lagrange equations. Numerical methods for the TV models in pixel domain can be adapted to these equations. For instance, one can solve them by the method of gradient flow [48], which is achieved by introducing an artificial time variable and solving the following equations to steady states for Model I and Model II respectively,

$$(\beta_{j,k})_t = \int \nabla \left(\frac{\nabla u}{|\nabla u|} \right) \psi_{j,k}(x) dx, \quad (j,k) \in I, \tag{15}$$

and

$$(\beta_{j,k})_t = \int \nabla \left(\frac{\nabla u}{|\nabla u|} \right) \psi_{j,k}(x) dx - 2\lambda_{j,k}(\beta_{j,k} - \alpha_{j,k}). \tag{16}$$

The steady states refer to $(\beta_{j,k})_t = 0$. In this case, gradient flows (15) and (16) are reduced to the Euler-Lagrange equations (8) and (9).

Many numerical schemes can solve the above equations. For instance, we now describe a simple explicit finite difference algorithm that we employ to find the minimizers in this paper. To simplify the formulation, we introduce the standard finite difference notations, such as the forward differences $D_1^+ u_{k,l} = u_{k+1,l} - u_{k,l}$,

$D_2^+ u_{k,l} = u_{k,l+1} - u_{k,l}$, and the backward differences $D_1^- u_{k,l} = u_{k,l} - u_{k-1,l}$, $D_2^- u_{k,l} = u_{k,l} - u_{k,l-1}$. The time step size is denoted by Δ_t and space grid size is $\Delta_x = \frac{1}{n}$. We also define $I_{j,k}$ as the characteristic function of inpainting regions I, i.e.

$$\chi_{j,k} = \begin{cases} 1 & (j,k) \in I \\ 0 & (j,k) \notin I \end{cases}$$

We note that it is important to evaluate the nonlinear term, which we denote as,

$$\text{WCURV} \equiv \int \nabla \left(\frac{\nabla u}{|\nabla u|} \right) \psi_{j,k}(x) dx$$

in both equations (15) and (16). This term is the curvature projected on the wavelet basis. However, the curvature is defined in the pixel domain. In this paper, we calculate it straightforwardly by transforming the coefficients to the pixel domain to compute the curvature, and then transform back to the coefficient domain. In detail, we calculate

$$u = \text{IWT}(\beta), \tag{17}$$

where IWT is the inverse wavelet transform. For all (i,j), compute

$$\begin{aligned} \text{curv}_{i,j} = D_1^- & \left(\frac{D_1^+ u_{i,j}}{\sqrt{|D_1^+ u_{i,j}|^2 + |D_2^+ u_{i,j}|^2 + \epsilon}} \right) \\ & + D_2^- \left(\frac{D_2^+ u_{i,j}}{\sqrt{|D_1^+ u_{i,j}|^2 + |D_2^+ u_{i,j}|^2 + \epsilon}} \right), \end{aligned} \tag{18}$$

where ϵ is a small positive number which is used to prevent the numerical blow-up when $\sqrt{|D_1^+ u_{i,j}|^2 + |D_2^+ u_{i,j}|^2} = 0$. In fact, this modification is the standard regularization technique described in Section 3.1. Then one computes the curvature projection on the wavelet basis by

$$\text{WCURV} = \text{FWT}(\text{curv}), \tag{19}$$

where FWT is forward wavelet transform.

The complete algorithm can be summarized by the following pseudo-code.

Algorithm:

(1) Start with $n = 0$ and initial guess $\beta_{j,k}^{new} = \alpha_{j,k} \chi_{j,k}$. Set $\beta_{j,k}^{old} = 0$, and the initial error $E = \|\beta^{new} - \beta^{old}\|_2$.

(2) While $i \leq N$ or $E \leq \delta$, do

- Set $\beta^{old} = \beta^{new}$.
- Calculate WCURV by (17), (18) and (19).
- For all (j,k), update

$$\beta_{j,k}^{new} = \beta_{j,k}^{old} + \frac{\Delta_t}{\Delta_x} \gamma_{j,k},$$

where $\gamma_{j,k}$ is defined by

$$\gamma_{j,k} = \beta_{j,k}^{TV} \chi_{j,k}$$

for Model I, and by

$$\gamma_{j,k} = \beta_{j,k}^{TV} - 2\lambda(\beta_{j,k} - \alpha_{j,k})\chi_{j,k}$$

for Model II respectively.

- Compute error $E = \|\beta^{new} - \beta^{old}\|_2$, and set $i = i + 1$.
- End the while loop.

5. Examples. To test the models, we use standard Peak Signal to Noise Ratio (PSNR) to quantify the improvements of performance of inpainting. PSNR is defined as

$$\text{PSNR} = 10\log_{10}(\frac{255^2}{\|u - u_0\|_2^2})(dB),$$

where 255 is the maximum intensity value of gray scale images, u_0 is the noise free original image, $\|\cdot\|_2$ the standard L^2 norm. As usual, the larger the PSNR value, the better the performance. In addition, we also show some of the image comparisons to illustrate the performance of restoring sharp edges and other geometric features, which cannot be reflected through PSNR measurement. In all examples shown here, we use Daubechies 7-9 biorthogonal wavelets with symmetric extensions at the boundaries.

In Model II, we determine the parameter λ by testing different values and selecting the visually best one among them.

In the first example, we apply our two models to a synthetic image shown on the left panel of Figure 2. The image contains different geometrical features with different intensity values. The picture in the middle is obtained by losing (setting to zero) 50% of its wavelet coefficients randomly, resulting in PSNR = $9.5(dB)$. As one can observe, there are no well defined inpainting regions in the pixel domain. The black parts of the right picture in Figure 2 show which coefficients are lost in the wavelet frequency domain. The frequencies are arranged in the standard manner with upper left corner storing the low-low frequencies, and lower right portion the high-high frequencies. Obviously, many of the low frequency coefficients are lost which results in the large black areas (with fuzzy boundaries) in the pixel domain. It is noticeable that most of the boundaries of the geometrical features are destroyed due to the loss of related wavelet coefficients. Moreover, different regions have different severity of damage which are certainly inhomogeneous in the image domain.

We show the inpainted image using Model I and Model II on the left and middle of Figure 3 respectively. In the computation using Model II, we set the parameter $\lambda = 10$. It is clear that both models can fill in the missing information properly, and restore the sharp edges and geometrical shapes surprisingly well. The PSNR are $29.4(dB)$ and $26.4(dB)$ for the left and middle respectively.

On the right picture of Figure 3, we show the performance improvement measured by PSNR v.s. the severity of the damage. The x-axis represents the percentage of wavelet coefficients being retained. Towards the right end, more coefficients are kept and less damage is introduced. The y-axis is the performance measured by PSNR. The curve with circles is obtained by using Model I in the reconstruction, while the curve with stars is drawn by using Model II. The figure shows several important properties of the proposed models. First of all, both models can improve the image quality dramatically. The improvement in PSNR is more than $10(dB)$ even if there are more than 70% wavelet coefficients are lost. The plot shows that the less damage to the wavelet coefficients, the larger the improvement in PSNR, which is to be expected.

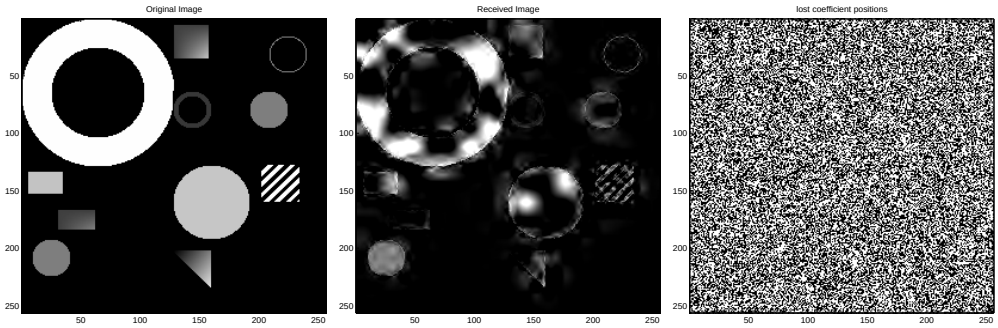

FIG. 2. *Left: Original synthetic image. Middle:* 50% *of the wavelet coefficients are randomly lost, including some low frequency coefficients, which results in large damaged regions in the pixel domain. Notice that there are no well defined inpainting regions in the pixel domain.* PSNR $= 9.5(dB)$. *Right: The index picture shows the locations (black) of missing wavelet coefficients. The upper left corner stores the low-low frequencies and the lower right portion the high-high ones.*

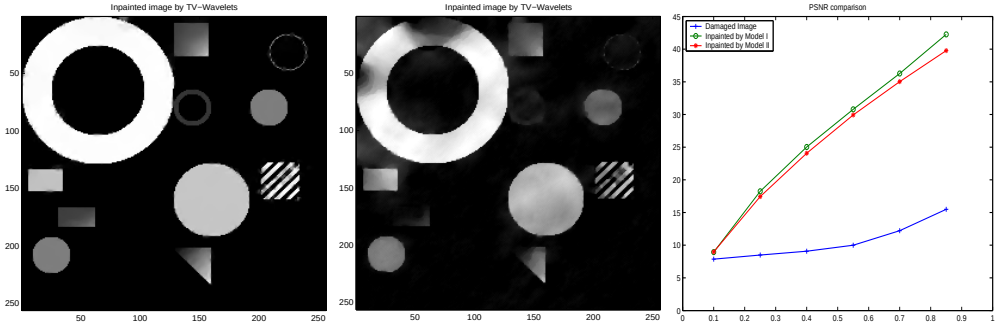

FIG. 3. *Restored images by Model I (left,* PSNR $= 29.4(dB)$*) and Model II (middle,* PSNR $= 26.5(dB)$*). They not only fill in missing regions properly, but also restore the sharp edges and geometrical shapes. The rightmost panel shows the performance comparisons of Model I and Model II with different level of damages. For the horizontal axis, for example,* $p = 0.85$ *means that* $1 - p = 15\%$ *of wavelet components are lost. The numerical curves in the rightmost panel show that both models can dramatically improve image qualities.*

The picture also indicates that for the noise free synthetic image, Model I outperforms Model II even though both can restore the image very well. However, comparing to the improvement over the damaged image, the difference between Model I and Model II is small.

In addition to the improvements measured by PSNR, as shown in Figure 3 both models improve the visual quality dramatically as well. For comparison purpose, we show a sequence of pictures with different percentages of randomly lost coefficients in Figure 4 and 5 The left images are the damaged images to be inpainted, the middle ones are inpainted by Model I and the right ones by Model II. In Figure 4, there are only 15% coefficients randomly lost, corresponding to the right ends of the curves shown in the PSNR comparison on the right panel of Figure 3. In Figure 5, the percentage of randomly lost coefficients is 90%, which corresponds to the left ends of the curves. As shown by the curves, if more coefficients are lost, the reconstruction improvements drop as well as the visual qualities.

To further compare the models, in addition to losing 50% coefficients randomly, we introduce Gaussian noise to the images as well. The picture with PSNR $= 9.2(dB)$

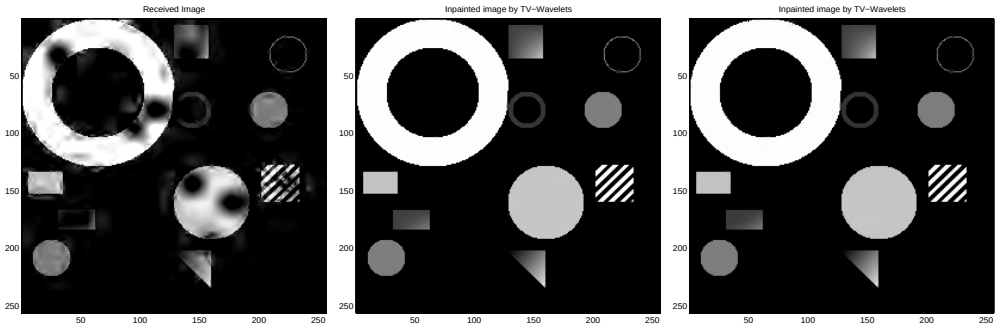

FIG. 4. *Left: Damaged image with* 15% *wavelet coefficients randomly lost. Restored images by Model I (middle,* PSNR = 42.3(dB)*) and Model II (right,* PSNR = 39.8(dB)*). Both inpainted images well agree with the original noise free image.*

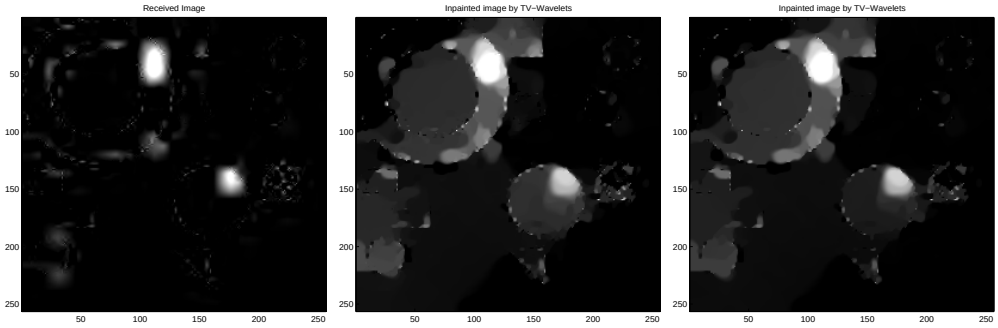

FIG. 5. *Left: Damaged image with* 90% *wavelet coefficients randomly lost. Restored images by TV wavelet image inpainting Model I (middle,* PSNR = 8.9(dB)*) and Model II (right,* PSNR = 9.0(dB)*). Both inpainted images can only restore partial geometry information since too many coefficients have been lost.*

is shown on the left panel of Figure 6. Both Model I and Model II are used to inpaint the missing regions and the results are displayed in the middle and right panel of Figure 6. The results clearly show that Model I can recover the geometrical features of the image, but can not suppress the noise in the reconstruction. The PSNR is improved to 15.1(dB). While Model II with parameter $\lambda = 10$ can perform both tasks of inpainting and denoising at the same time. The PSNR is 19.6(dB), which certainly outperforms Model I in the noise case. To complete the comparison, we plot the similar curves for PSNR improvements v.s. the percentage of retained coefficients for the noisy case and show them in Figure 7. As one can see, Model II outperforms Model I in the noise case, and Model I can not reduce the damage caused by the noise.

In the next experiment, we investigate the inpainting ability of the proposed models in an extreme situation. We apply Model I to a simple synthetic image, a perfect square, as shown in the left panel of Figure 8. Instead of dropping high frequency coefficients as the usual wavelet approximations do, because they are considered less important than the low frequency coefficients, we retain all of the high frequencies and set all but one coefficients in the low-low subband to zero. The resulting picture is shown on the right panel of Figure 8. The inpainted picture is shown on the left panel of Figure 9. We can see that even with only one low frequency coefficient kept, Model I can recover the square almost exactly with PSNR = 61.0(dB), which

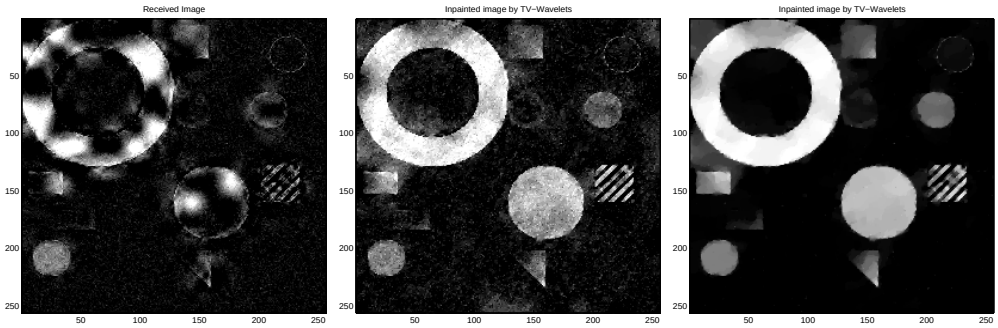

FIG. 6. *Left: A noisy image with* 50% *wavelet coefficients randomly lost. Middle: inpainted image by Model I. The geometrical features are restored, but the noise is not removed,* PSNR $= 15.1(dB)$. *Right: inpainted image by Model II with* $\lambda = 10$. *Notice how well the damaged geometrical features are restored and noise removed.* PSNR $= 19.6(dB)$.

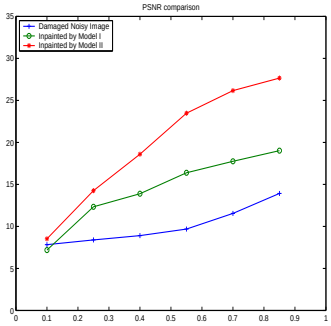

FIG. 7. *The performance comparisons of Model I and Model II with different level of damages for noisy images. It shows that both models can substantially improve image qualities while Model II can more effectively remove noises.*

is within the numerical error tolerance. On the right panel of Figure 9, we take a closer look at the inpainting by showing a cross plot of the recovered square. It is almost indistinguishable from the original square image. It shows that the proposed TV based inpainting model can recover the low frequency coefficients as well as the high frequencies successfully. Most existing inpainting models can not reconstruct huge loss in the low frequency subband.

After seeing the perfect recovery in the previous example, a natural question that arises is whether the models can perfectly reconstruct the square if all low frequency coefficients are lost. In Figure 10, we show such an example. The picture on the left is the damaged image, the inpainted image by Model I is shown in the middle, which looks like a perfect square. However, the intensity of the square is not the same as the original one. This can be seen clearly in the cross plot in the middle of the square shown on the right panel of Figure 10. The solid line is the original square. The dotted line is the damage image, which oscillates and loses all intensities in the middle of the square. The dash-dotted line is inpainted image by Model I. The intensity values are very different from the original ones. However, the inpainted image recovered the heights of the jumps. This can be explained by the different natures of the low and high frequency wavelet coefficients, as the high frequencies measure the variation information between neighboring pixels, while low frequencies collect their average

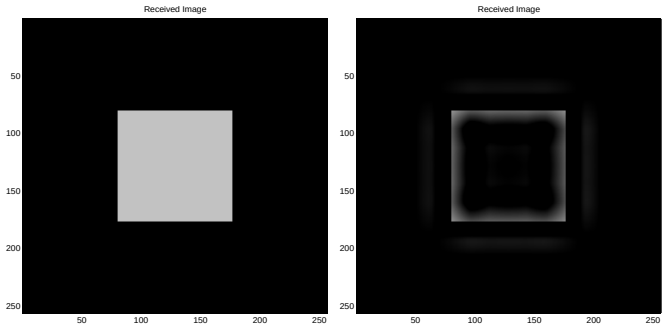

FIG. 8. *Left: An ideal image. Right: Damaged image with only one available non-zero coefficient in the low-low subband (but no loss in all other high resolution subbands).* PSNR $= 11.2(dB)$.

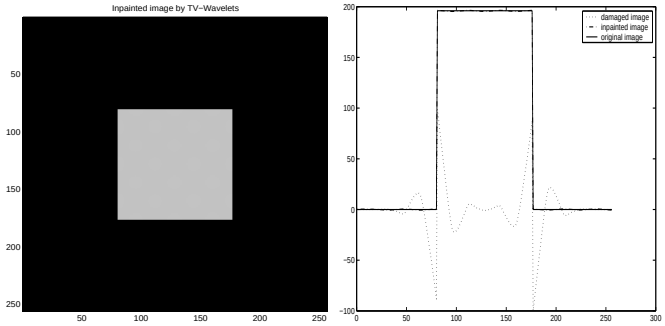

FIG. 9. *Left: The inpainted image by Model I. It almost perfectly recovers the square.* PSNR $=$ $61.0(dB)$. *Right: A horizontal slice of the inpainted image, which shows that the reconstruction coincides well with the original one.*

information. With all low frequencies being lost and all high frequency coefficients being retained in this example, the inpainting model can reconstruct the heights of the jumps, but can not uniquely determine their intensities, which can be different up to an arbitrary constant. However, if one retains any one nonzero low frequency coefficient as what we did in the previous example shown in Figure 9, the intensities can be uniquely determined, and the perfect recovery is obtained.

In the next set of examples, we apply the models to a real noisy picture (the left panel of Figure 11) downloaded from the Internet. Similar to the first example, 50% of the wavelet coefficients are randomly lost, including some low frequency coefficients (the right panel of Figure 11). The PSNR is $10.9(dB)$. Again, there are no well defined inpainting regions in this example. We show the restored images by using Model I (left) and II (right) in Figure 12. They fill in the black regions properly, and retain the sharp edges. Moreover, one can also observe that some detail information (such as the texture of the tie) is recovered surprisingly well. This is due to the retained high frequency wavelet coefficients which contain the fine structure. Their respective PSNR's are $18.8(dB)$ and $18.7(dB)$.

To further confirm the inpainting capability of the proposed models, we specially investigate the case where large regions in the low-low subband are lost. We show the picture on the left panel of Figure 13 with PSNR $= 13.1(dB)$. In this case, the standard inpainting methods cannot fill in the large missing region properly, while

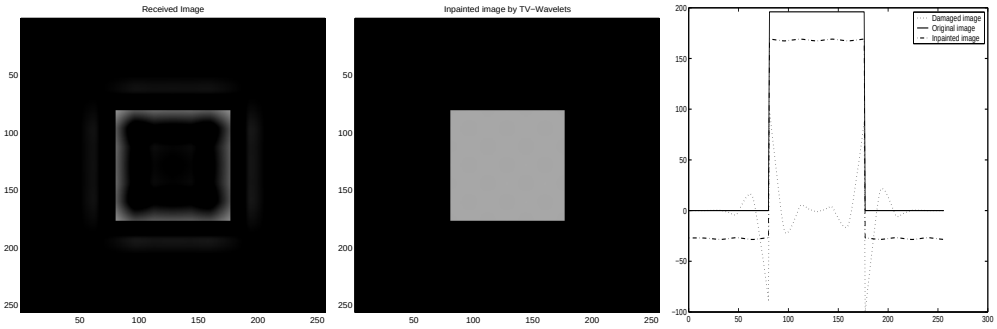

FIG. 10. *Left: The damaged image with all the low-low components missing (but no loss in all other high resolution subbands). Middle: The inpainted image by Model I, it looks like a perfect square is recovered, but their intensities are all wrong. Right: the cross plot of in the middle of the square of the inpainted image. The solid line is the original square, the dotted line is the damaged image and the dash-dotted line is the inpainted image. Clearly, the intensities are all wrong even thought the size of the jumps are perfectly reconstructed.*

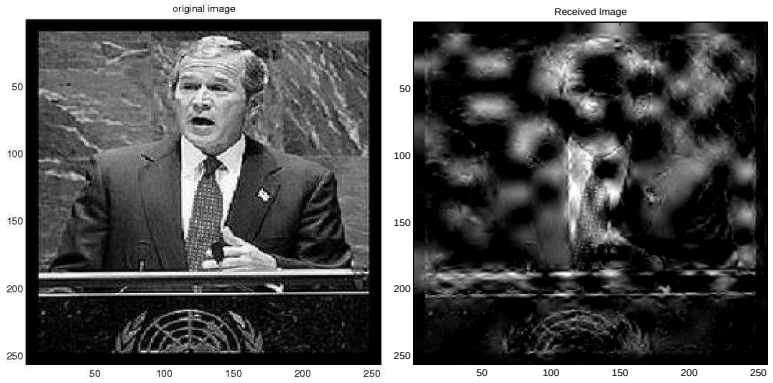

FIG. 11. *Left: Original noisy image. Middle:* 50% *of the wavelet coefficients are randomly lost, including some low frequency coefficients. Notice the severe damage in the pixel domain.* $\mathrm{PSNR} = 10.9(dB)$.

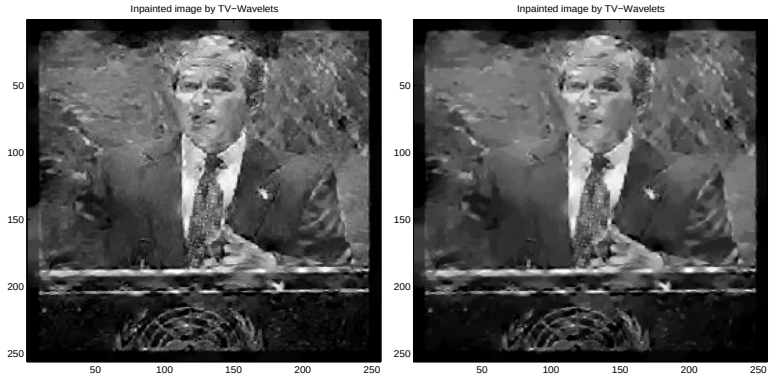

FIG. 12. *Restored images by Model I (left) and Model II (right). They both fill in the blank regions properly, and retain the sharp edges. One can even observe some detailed information such as the texture of the tie in the inpainted image. The corresponding* PSNR*'s are* $18.8(dB)$ *and* $18.7(dB)$ *separately.*

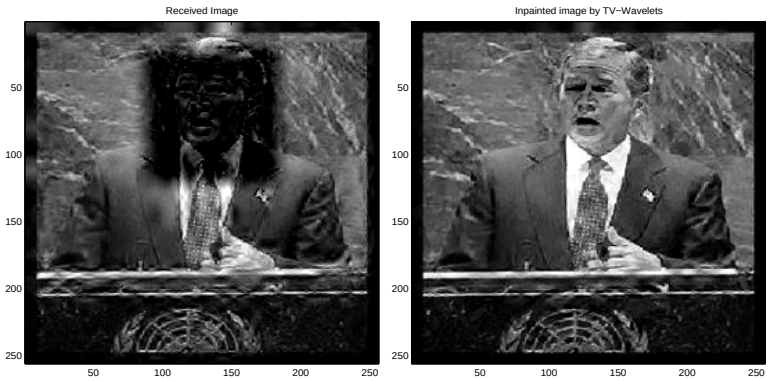

FIG. 13. *Left: Damaged image with a square region missing in the low-low subband, in addition to the randomly lost* 30% *high frequency coefficients.* PSNR $= 13.1(dB)$. *Right: Restored images by Model I.* PSNR $= 22.0(dB)$.

the proposed models can recover the image and improve the quality drastically. This is mainly because there is still some information available from the retained wavelet coefficients on the dark regions in the pixel domain. As seen on the right panel of Figure 13, we demonstrate the image obtained by using Model I. PSNR of the inpainted image is improved to $22.0(dB)$.

6. Conclusion. We have presented two models for restoring arbitrary number of coefficients with arbitrary locations of wavelet coefficients for images with or without noise. The idea is to use explicit given regularization in the pixel domain to control and restore wavelet coefficients in the wavelet domain. We have shown through synthetic and real images that both models are very effective for restoring geometric features as well as filling in smooth regions, even with relatively large number of lost coefficients.

REFERENCES

[1] C. Ballester, M. Bertalmio, V. Caselles, G. Sapiro and J. Verdera, *Filling-in by Joint Interpolation of Vector Fields and Grey Levels*, IEEE Trans. Image Processing, 10(8), 2001, 1200-1211.

[2] M. Bertalmio, A.L. Bertozzi, and G. Sapiro. *Navier-Stokes, fluid dynamics, and image and video inpainting*, 2001 IEEE Conference on Computer Vision and Pattern Recognition. December. Kauai, Hawaii. Available at http://www.ece.umn.edu/users/marcelo/final-cvpr.pdf.

[3] M. Bertalmio, G. Sapiro, V. Caselles and C. Ballester, *Image Inpainting,* Tech. Report, ECE-University of Minnesota, 1999.

[4] M. Bertalmio, L. Vese, G. Sapiro and S. Osher, *Simultaneous Structure and Texture Image Inpainting*, UCLA CAM Report 02-47, July 2002,

[5] E. Candès and D. Donoho, *Curvelets - A Surprisingly Effective Nonadaptive Representation for Objects with Edges*, Curves and Surfaces, L. L. Schumaker et al. Eds, Vanderbilt University Press, Nashville, TN. 1999.

[6] E. J. Candès, and F. Guo. *Edge-preserving Image Reconstruction from Noisy Radon Data*, (Invited *Special Issue of the Journal of Signal Processing on Image and Video Coding Beyond Standards.*), 2001.

[7] V. Caselles, R. Kimmel and G. Sapiro, *On Geodesic Active Contours*, Int. Journal of Computer Vision, 22(1), 1997, 61-79.

[8] A. Chambolle, R. A. DeVore, N.-Y. Lee, and B. J. Lucier. *Nonlinear wavelet image processing: variational problems, compression and noise removal through wavelet shrinkage.* IEEE Trans. Image Processing, 7(3):319–335, 1998.

[9] T. F. Chan, S. H. Kang and J. Shen, *Euler's Elastica and Curvature Based inpainting* SIAM J. Appl. Math., 63(2) (2002), 564-592.
[10] T. F. Chan and J. Shen, *Mathematical Models for Local Non-Texture Inpainting*, SIAM J. Appl. Math., 62(3) (2002), 1019-1043.
[11] T. F. Chan and J. Shen, *Morphologically Invariant PDE Inpaintings*, UCLA CAM Report 01-15, 2001.
[12] T. F. Chan, J. Shen, and L. Vese, *Variational PDE Models in Image Processing*, Notices of AMS, Vol 50, No. 1, January 2003.
[13] T. F. Chan and L. Vese, *Active Contour Without Edges* Submit to IEEE Tran. on Image Proc., 1998.
[14] T. F. Chan and C. K. Wong, *Total Variation Blind Deconvolution*, IEEE Trans. Image Processing, 7 (1998), pp. 370-375.
[15] T. F. Chan and H. M. Zhou, *ENO-wavelet Transforms for Piecewise Smooth Functions*, SIAM J. Numer. Anal., Vol 40, No. 4 (2002), 1369–1404;
[16] T. F. Chan and H. M. Zhou, *Total Variation Minimizing Wavelet Coefficients for Image Compression and Denoising*, submitted to SIAM Journal on Scientific Computing.
[17] T. F. Chan and H. M. Zhou, *Optimal Constructions of Wavelet Coefficients Using Total Variation Regularization in Image Compression*, CAM Report, No. 00-27, Dept. of Math., UCLA, July 2000.
[18] M. Y. Cheng, H. Y. Huang and A. W. Y. Su, *A NURBS-based Error Concealment Techniques for Corrupted Images from Packet Loss*, in Proc. ICIP, bf 2, 2002, pp705-708.
[19] A. Cohen, R. DeVore, P. Petrushev, and H. Xu. *Nonlinear approximation and the space $BV(R^2)$.* Amer. J. Math., 121:587–628, 1999.
[20] I. Daubechies. *Ten lectures on wavelets.* SIAM, Philadelphia, 1992.
[21] R. A. DeVore, B. Jawerth, and B. J. Lucier. *Image compression through wavelet transform coding.* IEEE Trans. Information Theory, 38(2):719–746, 1992.
[22] L. Demanet, B. Song and T. Chan, *Image Inpainting by Correspondence Maps: a Deterministic Approach*, UCLA CAM Report 03-40, August 2003.
[23] D. Dobson and C.R. Vogel, *Convergence of An Iterative Method for Total Variation Denoising*, SIAM Journal on Numerical Analysis, 34 (1997), pp. 1779-1971.
[24] D. L. Donoho. *De-noising by soft-thresholding.* IEEE Trans. Information Theory, 41(3):613–627, 1995.
[25] D. L. Donoho and I. M. Johnstone. *Ideal spacial adaption by wavelet shrinkage.* Biometrika, 81:425–455, 1994.
[26] D. Dugatkin, H. M. Zhou, T. F. Chan and M. Effros, *Lagrangian Optimization of A Group Testing for ENO Wavelets Algorithm*, Proceedings to the 2002 Conference on Information Sciences and Systems, Princeton University, New Jersey, March 20 - 22, 2002.
[27] S. Durand and J. Froment, *Artifact Free Signal Denoising with Wavelets*, in Proceedings of ICASSP'01, volume 6, 2001, pp. 3685-3688.
[28] S. Esedoglu and J. Shen. Digital inpainting based on the Mumford-Shah-Euler image model. *European J. Appl. Math.*, 13:353–370, 2002.
[29] W. H. Fleming and R. Rishel. *An integral formula for total gradient variation.* Arch. Math., 11:218–222, 1960.
[30] E. De Giorgi. *Complementi alla teoria della misura $(n-1)$-dimensionale in uno spazio n-dimensionale.* Sem. Mat. Scuola Norm. Sup. Pisa, 1960-61.
[31] E. Giusti. *Minimal Surfaces and Functions of Bounded Variation.* Birkhäuser, Boston, 1984.
[32] *Special Issue on Partial Differential Equations and Geometry-Driven Diffusion in Image Processing and Analysis*, IEEE Tran. on Image Proc., Vol. 7, No. 3, Mar. 1998.
[33] P. C. Hansen, *The L-curve and Its Use in the Numerical Treatment of Inverse Problems*, Tech. Report, IMM-REP 99-15, Dept. of Math. Model., Tech. Univ. of Denmark, 1999.
[34] S. S. Hemami and R. M. Gray, *Subband-coded Image Reconstruction for Lossy Packet Networks*, IEEE Trans. Image Proc., 6:4, Apr. 1997, pp 523-539.
[35] H. Igehy and L. Pereira, *Image Replacement Through Texture Synthesis*, Proceedings to IEEE ICIP, 1997.
[36] K.-H. Jung, J.-H. Chang, and C. W. Lee, *Error Concealment Technique Using Data for Block-Based Image Coding*, SPIE, 2308,(1994), 1466-1477.
[37] Sung Ha Kang, Tony F. Chan and Stefano Soatto, *Inpainting from Multiple View*, UCLA CAM Report 02-31, May 2002.
[38] E. H. Lieb and M. Loss. *Analysis.* Amer. Math. Soc., second edition, 2001.
[39] M. Masnou and J. Morel, *Level-lines Based Disocclusion*, IEEE ICIP, October, 1998, 259-263.
[40] D. Marr. *Vision.* Freeman, San Francisco, 1980.
[41] Y. Meyer. *Oscillating Patterns in Image Processing and Nonlinear Evolution Equations*, vol-

ume 22 of *University Lecture Series*. AMS, Providence, 2001.

[42] D. Mumford and J. Shah. *Optimal approximations by piecewise smooth functions and associated variational problems.* Comm. Pure Applied. Math., 42:577–685, 1989.

[43] Yan Niu and T. Poston, *Harmonic postprocessing to conceal for transmission errors in DWT coded images*. preprint, Institute of Eng. Sci., National Univ. of Singapore, 2003.

[44] J. W. Park and S. U. Lee, *Recovery of Corrupted Image Data Based on the NURBS Interpolation*, IEEE Trans. Circuits Syst. Video Tech., 9:7, Oct. 1999, pp 1003-1008.

[45] I. Peterson, *Filling in Blanks*, Science News, Vol. 161/19, May 11, 2002.

[46] S. Rane, J. Remus, and G. Sapiro, *Wavelet-domain reconstruction of lost blocks in wireless image transmission and packet-switched networks*. IEEE ICIP, 2002.

[47] S. Rane, G. Sapiro and M. Bertalmio, *Structure and texture filling-in of missing image blocks in wireless transmission and compression applications.* IEEE Trans. Image Processing 12, pp 296-303, 2003

[48] L. Rudin, S. Osher and E. Fatemi, *Nonlinear Total Variation Based Noise Removal Algorithms*, Physica D, Vol 60(1992), pp. 259-268.

[49] G. Sapiro, *Geometric Partial Differential Equations and Image Processing*, Cambridge University Press, 2001.

[50] G. Sapiro and A. Tannenbaum, *Affine Invariant Scale-Space*, Internet. J. Comput. Vision, 11 (1993), pp. 25-44.

[51] Y. Wang, and Q. F. Zhu, *Error Control and Concealment for Video Communication: A Review*, Proc. IEEE, vol 86, no. 5, pp. 974-997.

[52] A. Yezzi, A. Tsai and A. Willsky, *A Fully Global Approach to Image Segmentation via Coupled Curve Evolution Equations*, Submitted to Journal of Visual Communication and Image Representation.